Spectrochimica Acta Part A: Molecular and Biomolecular Spectroscopy 262 (2021) 120090

Contents lists available at ScienceDirect

Spectrochimica Acta Part A: Molecular and Biomolecular Spectroscopy

journal homepage: www.elsevier.com/locate/saa

Chemical constitution of polyfurfuryl alcohol investigated by FTIR and Resonant Raman spectroscopy

Francesco D'Amico [a,*], Maurizio E. Musso [b,*], Raphael J.F. Berger [b], Nicola Cefarin [a], Giovanni Birarda [a], Gianluca Tondi [c], Durval Bertoldo Menezes [d], Andreas Reyer [b], Letizia Scarabattoli [b,e], Thomas Sepperer [f,g], Thomas Schnabel [f], Lisa Vaccari [a]

[a] Elettra-Sincrotrone Trieste S.C.p.A., Strada Statale 14 – km 163,5 in AREA Science Park, 34149 Basovizza, TS, Italy
[b] University of Salzburg, Department of Chemistry and Physics of Materials, Jakob-Haringer-Strasse 2a, 5020 Salzburg, Austria
[c] Land, Environment, Agriculture and Forestry Department, University of Padua, Viale dell'Università 16, 35020 Legnaro, PD, Italy
[d] Federal Institute of Triângulo Mineiro, Campus Uberlândia, 38.400-970 Uberlandia, Minas Gerais, Brazil
[e] Università degli Studi di Perugia, Department of Chemistry, Biology and Biotechnology, Perugia, Italy
[f] Salzburg University of Applied Sciences, Forest Products Technology & Timber Construction Department, Marktstrasse 136a, 5431 Kuchl, Austria
[g] Salzburg Center for Smart Materials, Jakob-Haringer-Strasse 2a, 5020 Salzburg, Austria

HIGHLIGHTS

- Macroscopic properties of PFA depends from its degree of polymerization.
- Combined use of FTIR and Resonant Raman is fundamental to infer about PFA chemistry.
- PFA mainly polymerizes into linear non conjugated furan chains.
- Fully polymerized PFA does not contain conjugated blocks.

GRAPHICAL ABSTRACT

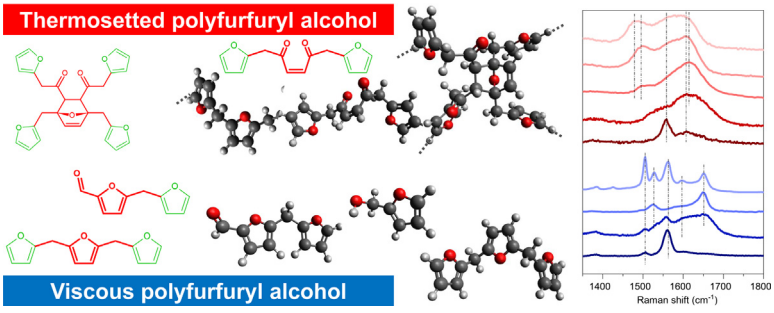

ARTICLE INFO

Article history:
Received 30 March 2021
Received in revised form 15 June 2021
Accepted 16 June 2021
Available online 18 June 2021

ABSTRACT

The actual chemical structure of polyfurfuryl alcohol (PFA) is still uncertain in spite of several studies on the topic, variations during the polymerization processes being one reason that must be addressed. The use of a limited set of analytical techniques is often insufficient to provide an exhaustive chemical characterization. Moreover, it is still not possible to exactly determine presence and amount of each specific functional group in the polymeric structure. We employed both Fourier Transform Infrared Spectroscopy (FTIR) and Resonant Raman spectroscopy (RR), corroborated by quantum mechanically aided analysis of the experimental spectra, to infer about the chemical structure of two samples of PFAs, synthetized in different ways and appearing macroscopically different, the first one being a liquid and viscous commercial sample, the second one being a self-prepared solid and rigid sample produced following a thermosetting procedure. The vibrational spectroscopic analysis confirms the presence of differences in their chemical structures. The viscous form of PFA is mainly composed by short polymeric chains, and is characterized by the presence of isolated furfuryl alcohol and furfural residues similar to 5-hydroxymethylfurfural; the thermosetted PFA is formed by more cross-linked structures, characterized by several ketones and alkene double bonds, as well as a significant presence of Diels-Alder structures.

* Corresponding authors.
E-mail addresses: francesco.damico@elettra.eu (F. D'Amico), maurizio.musso@sbg.ac.at (M.E. Musso).

https://doi.org/10.1016/j.saa.2021.120090

In summary, the present study evidences how the use of both FTIR and RR spectroscopy, the latter carried out at several laser excitation wavelengths, indicates an accurate way to spectroscopically investigate complex polymers enabling to satisfactorily infer about their peculiar chemical structure.

1. Introduction

In a world seeking for bio-based materials, polyfurfuryl alcohol (PFA) is one attractive solution because of its natural origin, coming from renewable resources [1,2], and due to its good mechanical and thermal properties [3]. Despite the facile polymerization, its chemical structure has not been investigated up to 1953, year of the first publication by Dunlop and Peters [4]. The monomer, furfuryl alcohol (F-OH), can be obtained from catalytic reduction of furfural, which in turn is obtained from hydrolysis and dehydration of carbohydrates, such as hemicellulose residues from sugarcane, rice or corncobs [5–7]. Due to its high dimensional stability, PFA is used as binder in foundry for sand moulding [8,9]. About its physicochemical properties, we can mention a very good thermal stability and a great resistance to acidic conditions [10]. In addition, when PFA is used in composite materials, its presence increases the mechanical properties of such materials, such as tensile, flexural, impact strength and storage modulus [11,12]

Recently, attractive bio-copolymers based on PFA, with excellent scientific and industrial interest, have been proposed. Among these we can mention: (a) Epoxidized linseed oil, Tung-oil and lactic acid copolymers, which have shown the possibility to synthetize bio-based plastics [13–15]; (b) Tannin-furanic foams, based on tannin-F-OH copolymers, which have shown outstanding features for the insulation of green building and have been also synthetized on industrial scale [16–18]; (c) lignin-furanic polymers, with good adhesive properties [10,19,20]; (d) the use of PFA in the preparation of corrosion-resistant glass fibre-reinforced composites and of carbon-based nanocomposites for applications into molecular sieve adsorbents and electrodes [21–24]; and (e) finally, the F-OH employment to produce innovative materials with enhanced stability, suitable for outdoor application in construction [25]. Overall, these products are attractive bio-based solutions to replace thermoset petrol-products such as polyurethanes, phenolic or amino-plastic adhesives and foams.

To understand the interaction of the various copolymers coupled with F-OH, a deeper insight to clarify its mechanism of polymerization is necessary. PFA is the product of the polycondensation of F-OH. This product is obtained by acid catalysis of liquid pale-yellow furfuryl alcohol, which turns quickly into a black rigid solid in a sort of explosion due to the high exothermicity of the process. This fascinating reaction has attracted the interest of many scientists to unscramble its complex chemistry. Most of the studies agreed with the presence of linear chains, originally presented by Dunlop & Peters [4], but then also other interesting adducts were hypnotized to justify the spectroscopic information collected over the years.

In particular, Conley & Metil introduced the possibility of ring-opening [26], Wewerka suggested the termination of the chain through α,β unsaturated γ lactones [27], Chuang et al. [28] proposed the methylene bridge between linear furanic chains, and finally Choura et al. proposed the crosslinking through Diels - Alder reaction [21].

More recent observations through ^{13}C NMR, FTIR and Raman spectroscopy have allowed to partly understand the proportion of the different structures when the polymer is completely polymerized [29–33]. Our study [29] was however considering exclusively the fully cured PFA polymer, i.e. a PFA thermoset in which a crosslinking reaction has occurred promoting chemical bonding between macromolecular chains and creating a three-dimensional network.

In this article we aim to extend the knowledge on the chemical constitution of PFA, by comparing a standard, commercially available, viscous PFA (*visc*-PFA) [34] and a self-prepared PFA that underwent a thermosetting procedure during its synthesis (*ThS*-PFA) [29]. The liquid and viscous character of *visc*-PFA suggests that it could be in an intermediate state, where the polymerization process has not been already completed, while in a previous study [29] we demonstrated that in *ThS*-PFA the thermosetting procedure completes the polymerization process, since residual F-OH was not present in the final solid and rigid polymer sample.

With the aim of discovering differences in the chemical constitutions of *visc*-PFA and *ThS*-PFA, we performed an extensive vibrational spectroscopic study of these two materials. We employed both FTIR spectroscopy and Raman spectroscopy at the excitation wavelengths of 1064 nm, 532 nm, 455 nm and Resonant Raman (RR) spectroscopy at the excitation wavelengths of 355 nm, 266 nm and 244 nm, in order to cover the whole RR landscape potentially exploited by PFA. Due to the complex chemical conformation characterizing both PFA samples, the spectral interpretation is supported by quantum mechanical simulations providing the vibrational profiles of the specific functional groups which are supposed to constitute the building blocks of the polymeric structures.

The work is organized as follows: Section 2 describes the sample preparation procedure, the experimental details adopted to get the final FTIR and Raman and RR spectra, as well as the description of the computational models adopted to generate the simulated spectra. Section 3 reports the experimental FTIR, Raman and RR spectra of *visc*-PFA and *ThS*-PFA, and Section 4 provides a detailed comparison between the theoretical and experimental results obtained.

2. Experimental section

2.1. PFA sample preparation

Thermosetted PFA (*ThS*-PFA) was prepared as described in Ref. [29]. Briefly: 0.1 mL of sulfuric acid (Merck) 32% was added in an open test tube containing 2 mL F-OH (Transfuran chemicals, Geel, Belgium). After 60–80 s the polycondensation reaction was completed and the PFA obtained was further kept in an oven at 103 °C for 1 h to complete the curing before grinding it into fine powder. This powder was leached with water to remove the catalyst and the unreacted F-OH, and then dried again at 103 °C until constant weight. The material resulted almost completely insoluble (only 2% was leached out) and the resulting dried black powder was the subject of this study.

Viscous PFA (*visc*-PFA) was purchased from Polyscience [34] and used as it is. The supplier declares that its product is composed by 90–95 % of 2-furanmethanol homopolymer and by a 5–10% of furfuryl alcohol. The sample appears as a black viscous liquid. The supplier declares a viscosity of (14500 ± 2500) cP.

2.2. FTIR

Attenuated Total Reflectance (ATR) Fourier Transform InfraRed (FTIR) spectra were acquired to characterize both PFA samples in

the MIR-FIR spectral range. To do so, the *ThS*-PFA (crushed into powder) and the *visc*-PFA were put onto the diamond internal reflection element of the Platinum ATR setup (Bruker Optics) housed in the in-vacuum Vertex 70v interferometer (Bruker Optics). Then the chamber was evacuated in order to limit the atmospheric water contribution. For each formulation, five different spectra were collected in the 6000–50 cm^{-1} spectral range, with 256 scans (both for the background and the sample), a spatial resolution of 2 cm^{-1} and at a frequency of 5 Hz. The five recorded spectra were averaged and cut in the 4000–400 cm^{-1} range, baseline corrected with the concave rubberband method (number of iterations = 5, and number of baseline points = 64) and both vector normalized and offset corrected in the whole range.

2.3. Raman

Raman measurements with laser excitation at 1064 nm, 532 nm, 455, nm, and 355 nm were carried out with the Raman instrumentation available at the Core Facility Spectroscopy of the University of Salzburg, collecting all the Raman spectra in backscattering configuration. A Bruker FTIR IF66 spectrometer equipped with a Raman module FRA106 was used for the Raman measurements at 1064 nm, with a laser power of 100 mW and a laser spot diameter of 100 μm. For the Raman measurements at 532 nm and 455 nm a Thermo Fisher Scientific DXR2 Raman microscope was used, recording the Raman spectra with a laser power of 1 mW, and using a 10 × objective delivering a laser spot diameter of approximately 2 μm. To avoid photodegradation during a prolonged measurement on a single sample spot, a Raman mapping with a step size of 10 μm was utilized, averaging approximately 300 spectra to a resulting spectrum. For the Raman measurements at 355 nm a Raman spectrometer MonoVista CRS + from the company S&I (Acton SP2750 spectrometer with LN2 cooled Princeton Instruments CCD camera) equipped with an Olympus BX51WI microscope and a 10 × UV objective was used, recording the Raman spectra with a laser power of 1 mW on a laser spot with approximately 2 μm in diameter. To avoid photodegradation during a prolonged measurement on a single sample spot, the sample was continuously oscillated with approximately 1–2 Hz and a path length of approximately 10 mm.

2.4. UV resonant Raman

UV resonant Raman measurements with laser excitation at 266 nm and 244 nm were carried out at the IUVS beamline of the Elettra Sincrotrone Trieste synchrotron radiation facility. A detailed description of the experimental apparatus can be found in Ref. [35]. The Raman scattered signal was collected in backscattering configuration, sending the scattered light to a single stage Czerny-Turner spectrometer (Princeton Instruments), with focal length of 750 mm, equipped with a 1800 lines/mm holographic grating and a Peltier-cooled back thinned CCD (Princeton Instruments). To avoid photodegradation during the measurements, the samples were continuously oscillated with 1 Hz frequency and a path length of 5 mm.

2.5. Theoretical spectra modelling

UV–visible absorption spectra of furfuryl alcohol (F-OH) have been calculated by means of the time dependent DFT calculations [36,37] carried out with the Orca software package [38,39] exploiting the hybrid density functional theory (DFT) model of Becke and co-authors [40–42] and the Lee–Yang–Parr exchange–correlation function [43,44]. The simulated molar extinction coefficient spectrum has been obtained by

$$\varepsilon\left(\tilde{\nu}\right) = \sum_i \frac{\sqrt{\pi}e^2N}{1000 * \ln(10)c^2m_e}\frac{f_i}{\sigma}exp\left[-\left(\frac{\tilde{\nu} - \tilde{\nu}_i}{\sigma}\right)^2\right]$$

where $\varepsilon\left(\tilde{\nu}\right)$ is the extinction coefficient at the energy of $\tilde{\nu}$ expressed in wavenumber, e and m_e are respectively the electron charge and its mass, c is the speed of light, N is the Avogadro's number and σ = 1600 cm^{-1} (0.2 eV) is a broadening factor [45]. The quantity f_i is given by the following equation

$$f_i = \frac{8\pi^2\,\tilde{\nu}\,m_e c}{3he^2}D_i$$

and can be considered as the oscillator strength (dimensionless) of each excited state induced by the electronic transitions, while D is the induced dipole strength in esu^2cm^2 and h is the Planck constant [45].

The computation of FTIR, Raman and RR spectra has been carried out using the Turbomole program package [46]. To get a good compromise between computational accuracy and computational costs, the BP-86 local density functional together with the Karlsruhe def2-SVP basis sets was used. The simulated FTIR spectral lineshapes were calculated through the sum of several Voigt profiles centred at the wavenumbers obtained by the simulations (one Voigt profile for each normal mode). Each Voigt profile has its area proportional to T^2, i.e. to the square of the change of the dipole moment along a given vibrational mode [38]. Otherwise differently indicated, we chose a Gaussian Full Width at Half Maximum (FWHM) = 10 cm^{-1} and a Lorentzian FWHM = 5 cm^{-1}.

As done for the FTIR, the simulated Raman spectral lineshapes were calculated by using Voigt profiles centred at the wavenumbers obtained by the simulations and with areas proportional to

$$A_i = \sqrt{\left(R_{T,T} + R_{II,II}\right)^2}$$

where $R_{T,T}$ and $R_{II,II}$ are the differential Raman scattering cross sections calculated considering the electric field vectors polarized orthogonal (T,T) and parallel (II,II) to scattering plane [47,48]. Such cross sections refer to an absolute temperature T = 298.15 K and to exciting radiations corresponding to the employed experimental Raman excitation wavelengths (i.e. 1064 nm, 532 nm, 455 nm, 355 nm, 266 nm and 244 nm).

To verify if the adopted models are appropriate to obtain a reliable description of PFA electronic transitions, we have compared the simulated FTIR, Raman and UV–vis absorption spectra of F-OH with the experimental ones, this comparison being illustrated in detail in the Supplementary materials. Comparisons of the simulated RR spectra of F-OH with the experimental ones indicate that the proposed model is able to predict with good accuracy the peak positions and the spectral intensity of the normal modes regarding C = C stretching inside the furan rings in the wavenumber region between 1300 and 1700 cm^{-1}. Conversely, between 800 and 1300 cm^{-1} the accuracy in the calculated peak position is reduced, being underestimated by 20 to 40 cm^{-1}, depending on the analysed normal mode, while the order of magnitude of the simulated peak intensities is preserved.

2.6. Model structures for computations

Because of the PFA chemical structure complexity, an accurate interpretation of the vibrational spectra carried out both with FTIR, Raman and RR requires the identification of which functional groups can origin the vibrational peaks experimentally observed. To avoid misinterpretation in the peak assignation, the way we followed was to compare the outcome of the experimental spectra

with targeted simulation of FTIR, Raman and RR vibrational spectra carried out on specific building blocks of PFA. In particular, for the interpretation of the RR spectra, it is fundamental to understand at which energies the main functional groups present in PFA have electronic transitions, thus leading to an enhancement of the Raman cross section. However, the impossibility to get experimental UV–vis absorption spectra of PFAs, because of the macroscopic characteristic of the samples, made the simulated UV–vis absorption spectra the only possible way to infer about electronic transitions in PFA. Following the indications of Refs. [29,30,49] we identified few chemical structures which reasonably are mostly present in the PFA polymers, i.e. the "building blocks" of the PFA themselves.

These chemical structures considered in the present work, and for which we performed quantum mechanical computations of UV–vis and vibrational spectra, are shown in Fig. 1, identifying the internal section of the structural units in red and the external ones in green, since in the comparison between experimental and simulated spectra we have to take care to disentangle the normal modes involving vibration in the central part of the simulated structural units (red) with respect to the lateral ones (green). By this way it will be possible to distinguish the vibrations associated to possible central structural units of PFA from the ones of terminal building blocks or artifacts of the model.

In the following we refer to these structures shown in Fig. 1 as *Lin*, *RingOp*, *StructFFL*, *Struct5HMF*, *DielsAlder*, and *Conj*.

3. Results

3.1. Experimental FTIR spectra

The experimental FTIR spectra of *Ths*-PFA and of *visc*-PFA are shown in Fig. 2. A qualitative comparison evidences several similarities between the two curves, in particular in the wavenumber range of 1500–1800 cm^{-1}, as well as similarities with the PFA FTIR spectra found in literature [29,31,32,49]. It is important to highlight the presence of a shoulder at 1690–1670 cm^{-1} in the *ThS*-PFA, missing in *visc*-PFA, while, on the contrary, *visc*-PFA shows a shoulder at around 1750 cm^{-1}, missing in *ThS*-PFA. It is also noteworthy the presence, at around 1012 cm^{-1} in the *ThS*-PFA FTIR spectrum and at around 1013 cm^{-1} in the *visc*-PFA FTIR spectrum, of a common sharp peak (i.e. FWHM ≈ 25 cm^{-1}). Relevant spectral profiles differences can be otherwise observed in the spectral range 650–850 cm^{-1} (blue square in Fig. 2), 1050–1250 cm^{-1} (red square in Fig. 2), and 3200–3700 cm^{-1} (green square in Fig. 2), where a broad OH-stretching band appears near 3400 cm^{-1} in the *visc*-PFA FTIR spectrum, but not in the *ThS*-PFA one. Other differences between the spectra are the presence in the *visc*-PFA FTIR spectrum of very sharp peaks (FWHM 12 cm^{-1}) centred at around 885, 1149 and 1505 cm^{-1}, these peaks being still present also in *ThS*-PFA, but with strongly reduced intensities (see also [29,31,32,49]).

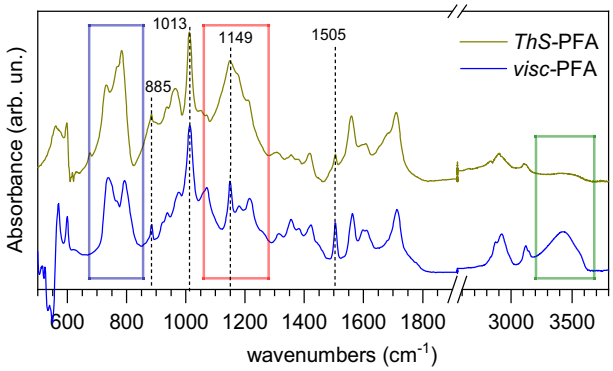

Fig. 2. FTIR spectra of *ThS*- and *visc*- PFA recorded in the spectral ranges 500–1900 cm^{-1} and 2600–3800 cm^{-1}.

3.2. Experimental Raman and resonant Raman spectra

In Fig. 3 the Raman spectra of both *visc*-PFA and *ThS*-PFA are compared in the spectral ranges 800–1350 cm^{-1} (panel a) and 1350–1800 cm^{-1} (panel b), collected at different laser excitation wavelengths spanning from 1064 nm to 244 nm. The spectra collected exploiting laser excitation sources in the near-IR and visible evidence clear differences between *visc*-PFA and *ThS*-PFA. In the near-IR region (excitation wavelength of 1064 nm) a clear Raman spectrum of *visc*-PFA was obtained, characterized by well-defined peaks centred at around 1385, 1425, 1506, 1528, 1563, 1597 and 1650 cm^{-1}, and free of any fluorescence contribution. On the contrary, for *visc*-PFA it was not possible to collect Raman spectra exploiting excitation sources in the visible at 532 nm and 455 nm, because both Raman profiles were hidden by an intense fluorescence background that overwhelmed any spectral features.

Differently to what occurs with *visc*-PFA, laser light absorption at the excitation wavelength of 1064 nm and related thermal dam-

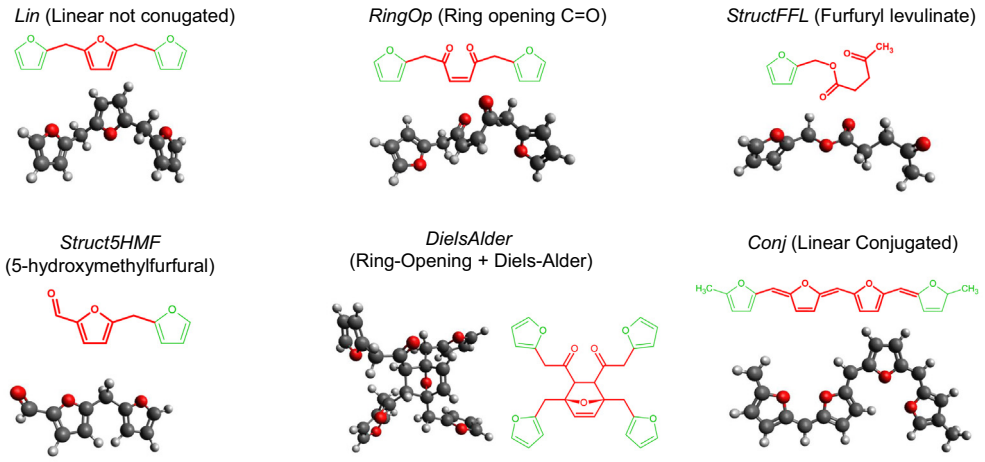

Fig. 1. Graphical representation of the simulated chemical structure, namely *Lin* (Linear not conjugated), *RingOp* (Ring opening + C = O), *StructFFL* (furfuryl levulinate derivative structure), *Struct5HMF* (5-hydroxymethylfurfural), *DielsAlder* (Ring opening + Diels-Alder), and *Conj* (Conjugated), identifying any internal portion of the chemical structures in red and any lateral one in green. The 3D layout is the result of the geometry optimization carried out by the simulations.

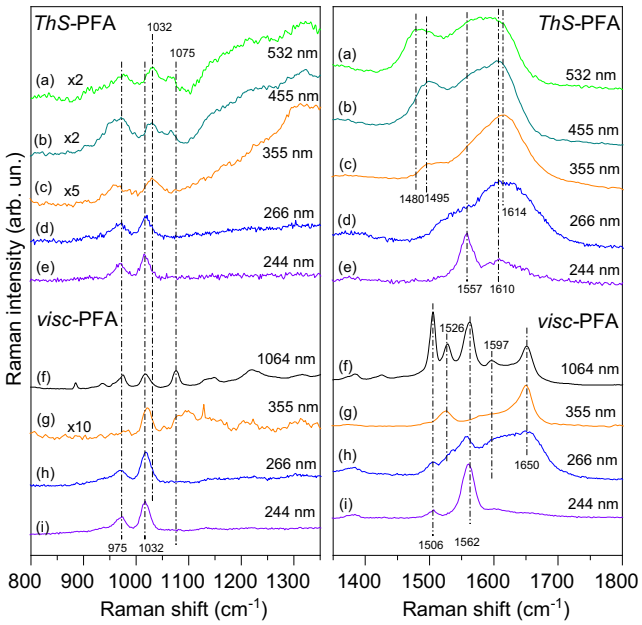

Fig. 3. Raman spectra of *visc*-PFA and *ThS*- PFA collected at excitation wavelengths of 1064 nm, 532 nm, 455 nm, 355 nm, 266 nm and 244 nm.

age impeded getting any Raman spectrum of *ThS*-PFA at this laser wavelength, while reliable *ThS*-PFA Raman spectra were obtained employing excitation wavelengths of 532 nm and 455 nm, after the application of a careful background subtraction procedure as done by Reyer et al. in Ref [18].

The Raman spectra of *ThS*-PFA recorded with 532 nm and 455 nm laser excitation differ greatly from the one of *visc*-PFA recorded with 1064 nm laser excitation, the *visc*-PFA spectrum being characterized by well-defined and sharp peaks, while the 532 nm and 455 nm *ThS*-PFA spectra being dominated by broadened spectral features centred near 1480 cm^{-1} and 1610 cm^{-1} in absence of any well-defined sharp peak.

At the excitation wavelength of 355 nm, the Raman spectra of both *visc-PFA* and *ThS*-PFA change their spectral profiles compared to the ones recorded at longer excitations wavelengths. The *visc*-PFA spectrum contains two well defined peaks: the most intense is centred at around 1650 cm^{-1} while a smaller one is centred at around 1526 cm^{-1}. On the contrary, the *ThS*-PFA spectrum is dominated by a broad feature at around 1614 cm^{-1} and a smaller one at around 1495 cm^{-1}. It is important to remark how our *visc*-PFA Raman spectrum with laser excitation at 355 nm strongly resembles the one obtained by Kim et al. from their self-prepared PFA with laser excitation at 325 nm [30], while the spectral profile of *ThS*-PFA behaves in a completely different way. The reason of such strong variations in the spectral lineshape will be discussed in detail in the following and is related to the different degree of polymerization of the two PFAs, and consequently to their different chemical composition.

Moving to 266 nm excitation wavelength, the spectral profiles continue to change, both for the *visc*-PFA and for the *ThS*-PFA. The spectra resemble the ones obtained at 355 nm, but with the appearance of two additional peaks at around 1506 cm^{-1} and 1562 cm^{-1} for *visc*-PFA, and of an additional spectral feature at around 1550 cm^{-1} for the *ThS*-PFA, these peaks becoming dominant in the spectra obtained at an excitation wavelength of 244 nm. It is important to note how, at this excitation wavelength, the *visc*-PFA and *ThS*-PFA Raman spectra result to be quite similar to each other, although with slight differences in peak positions.

In the wavenumber region of the Raman spectra between 800 and 1350 cm^{-1}, we note how the spectra at excitation wavelengths of 266 nm and 244 nm for both *visc*-PFA and *ThS*-PFA result to be very similar, being characterized by a doublet with peaks centred at around 975 cm^{-1} and 1017 cm^{-1}. Moving to visible excitations the spectra become noisier, because of the presence of fluorescence and the related background subtraction procedure, not allowing a good accuracy in the peak intensities. Anyway, we can observe that in both the PFAs a new peak seems to rise near 1075 cm^{-1} and a bump at around 1032 cm^{-1} seems to emerge in the Raman spectrum of *ThS*-PFA at 532 nm excitation wavelength. The peak at around 1075 cm^{-1} becomes clearly evident in the Raman spectrum of *visc*-PFA at 1064 nm excitation wavelength, where the fluorescence is strongly damped.

4. Discussion

4.1. UV–visible absorption spectra computations

As described in the experimental section, we have simulated the UV–vis absorption spectra of the model structure described above. The simulated spectra are reported in Fig. 4. The simulations evidence the presence of electronic transitions above 300 nm in *RingOp*, *Struct5HMF, DielsAlder* and *Conj*. Apart from the peculiar case of *Struct5HMF*, such transitions happen when an alkenes C = C bond outside the furanic ring occurs. On the contrary, furan rings alone, without the presence of alkenes in the backbone, seem not to generate such transitions. This evidence suggests that the differences between the Raman spectral profiles of *visc*-PFA and *ThS*-PFA occurring with 355 nm laser excitation are induced by these electronic transitions, that lead to resonance Raman effects. Below 250 nm, the absorption spectra result in the overlapping on many electronic transitions and the model adopted becomes less accurate since the model building blocks are too small to realistically simulate the electronic levels inside a polymeric structure.

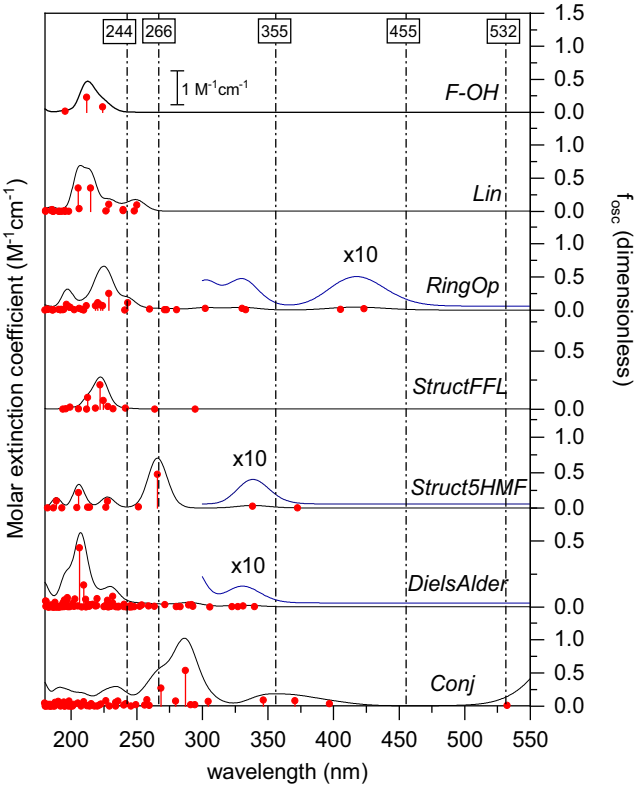

Fig. 4. Simulated UV–visible absorbance spectra in the wavelength range of 180 – 550 nm, carried out on F-OH *Lin*, *RingOp*, *StructFFL*, *Struct5HMF, DielsAlder*, and *Conj*.

However, within the strong limitations due to the extremely simplified model, these simulations can be interpreted in a qualitative way, indicating that the differences in the experimental Raman spectra are reasonable and can be qualitatively assigned as follows: the ones at 355 nm to resonance occurring with alkenes and in general with π-type bonds in the polymer backbone, while the ones at 266 nm and 244 nm to resonance occurring inside the furan rings. Therefore, with a good degree of confidence we can consider (see Fig. 3) the Raman peaks in resonance at 355 nm addressed to inter furan rings normal modes (i.e. the cross-linked structures) and the ones resonant at 244 nm to intra furan rings normal modes. Concluding, the 1064 nm, 532 nm and 455 nm Raman spectra in the spectral range between 1400 and 1800 cm^{-1} are constituted by an overlapping of all the normal modes (non-resonant and resonant), while from 355 nm to 244 nm laser excitation the PFA Raman spectral profiles become dominated by resonant vibrational modes, the Raman spectra with 266 nm laser excitation looking like a transition stage between the resonant normal modes.

4.2. Comparison between experimental and theoretical FTIR spectra

Fig. 5 presents a comparison between the FTIR spectra of *visc*-PFA and of *ThS*-PFA, already shown in Fig. 2, and the simulated FTIR spectra obtained from the chemical structures *Lin*, *RingOp*, *StructFFL*, *Struct5HMF*, *DielsAlder* and *Conj* shown in Fig. 1. In red the spectrum produced by the central portion of the chemical structures is identified, while in green the spectrum produced by the lateral moieties. This comparison evidences how the experimental peak at around 1012 cm^{-1} in *ThS*-PFA and at around 1013 cm^{-1} in *visc*-PFA can be addressed to the normal modes of the central part of the *Lin* structure, having the calculated wavenumbers at around 999.7 cm^{-1} and 1003.5 cm^{-1} associated to the C-H bending within the *Lin-C* furan rings.

As already mentioned above, the presence of some spectral differences between *visc*-PFA and *ThS*-PFA indicates differences in the two polymerized chemical structures. As seen in Fig. 5, the presence of a distinct peak at around 1000 cm^{-1} in the FTIR spectra indicates how *Lin-C* is the prevalent structure in both the PFAs.

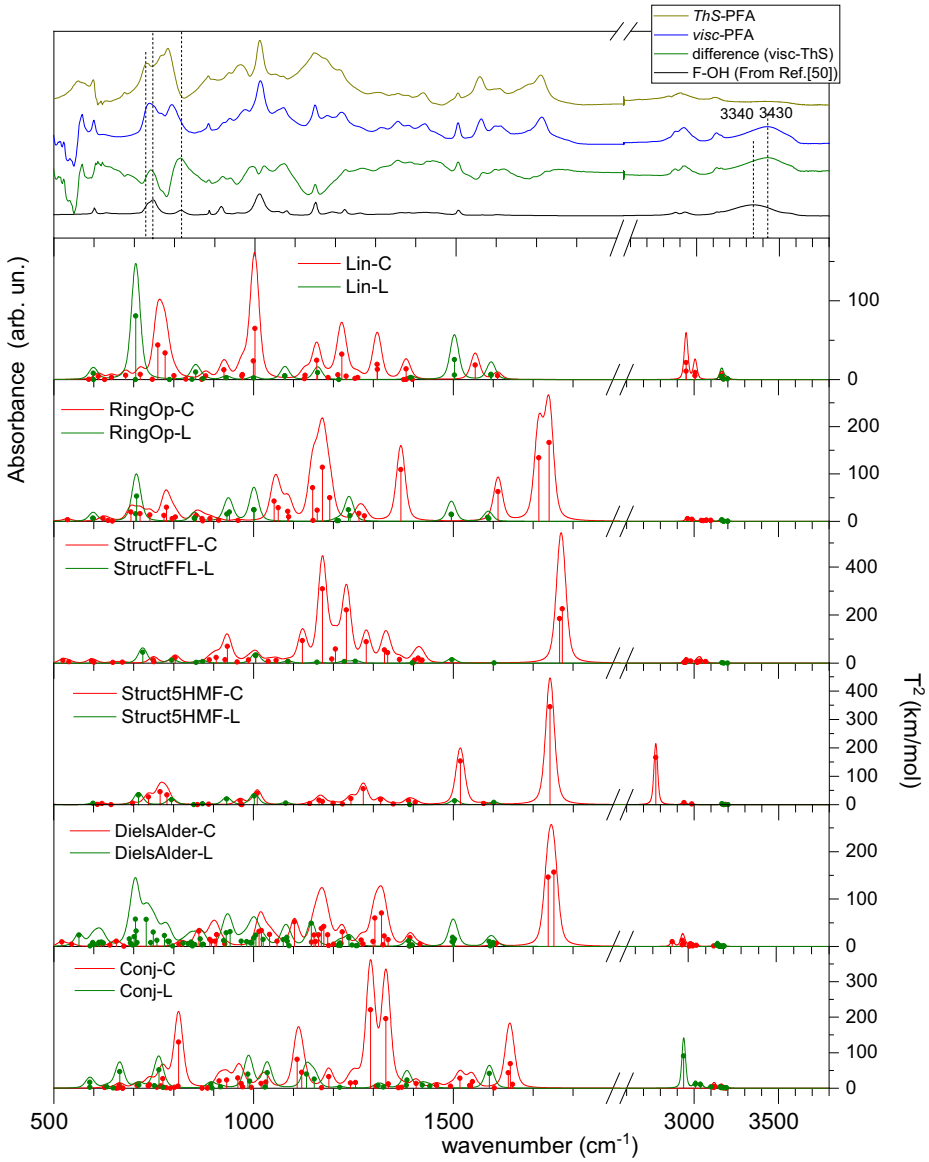

Fig. 5. Comparison of the experimental FTIR spectra of *visc*-PFA and of *ThS*-PFA in the wavenumber range of 500–1900 cm^{-1} and 2600–3800 cm^{-1}, shown on the top, with the simulated FTIR spectra obtained from the chemical structures *Lin*, *RingOp*, *StructFFL*, *Struct5HMF*, *DielsAlder* and *Conj* shown in Fig. 1, identifying in red the spectrum produced by the central (*-C*) portion of the chemical structures and in green the spectrum produced by the lateral (*-L*) one. The F-OH spectrum has been taken from Ref. [50].

To shed light about the other possible structures that could be present, we tentatively calculated the spectral difference between *ThS*-PFA and *visc*-PFA after a FTIR spectra normalization with the peaks at around 1000 cm^{-1}. Such spectral difference is shown in the upper panel of Fig. 5. The comparison with the simulated spectra allows to address the nature of the sharp peaks in *visc*-PFA spectrum centred at 885, 1149 and 1505 cm^{-1}. Basically, it must be noted how these peaks coincide with the ones of F-OH (see top panel of Fig. 5). Additionally, the top panel of Fig. 6 evidences the presence of an OH stretching hydroxyl band which can be easily addressed to the presence of F-OH, in accordance with the PFA characteristics given by the supplier [34]. There are small differences in the hydroxyls OH stretching band lineshapes between *visc*-PFA and F-OH: the first one is peaked around 3430 cm^{-1}, resembling the signal observed by Ipakchi and co-workers [51], the F-OH one instead at 3340 cm^{-1}. Such differences can be addressed to the different hydrogen bonding environment experienced by the hydroxyls in *visc*-PFA and F-OH, respectively. Since the 3430 cm^{-1} band disappears in the *ThS*-PFA spectrum, we can deduce that the thermosetting process suppresses the hydroxy groups as well as the residual water amount, if present.

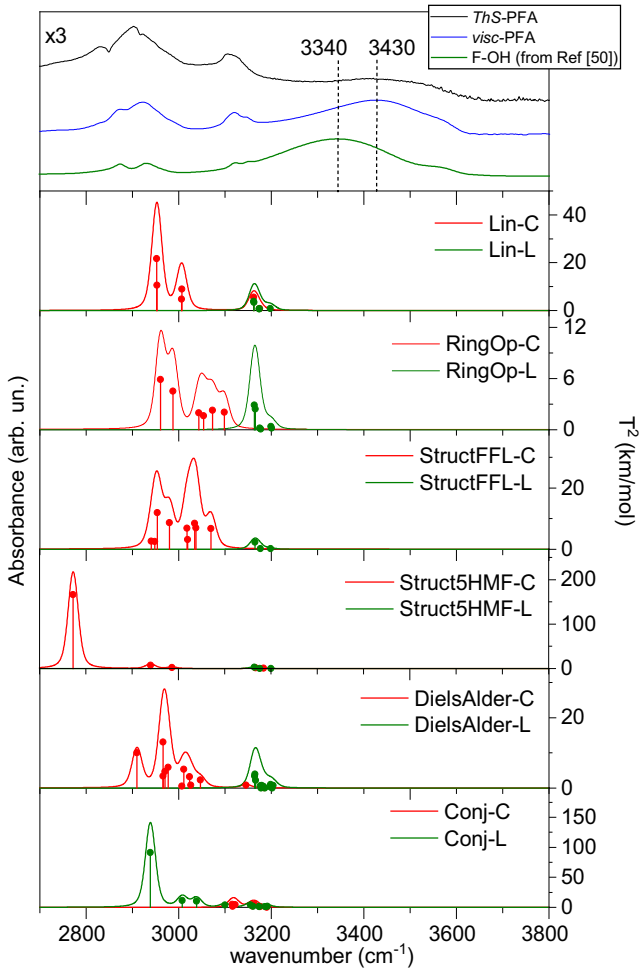

Fig. 6. Comparison of the experimental FTIR spectra of *visc*-PFA, *ThS*-PFA and F-OH in the wavenumber range of 2700–3300 cm^{-1}, shown on the top, with the simulated FTIR spectra obtained from the chemical structures *Lin*, *RingOp*, *StructFFL*, *Struct5HMF*, *DielsAlder* and *Conj* shown in Fig. 1, identifying in red the spectrum produced by the central (*-C*) portion of the chemical structures and in green the spectrum produced by the lateral (*-L*) one. The F-OH spectrum has been taken from Ref. [50].

The peaks at 885, 1149 and 1505 cm^{-1} can be also assigned to normal modes inside the furan ring linked on the lateral side of the polymer structure, i.e. *Lin-L, RingOp-L, StructFFL-L, Struct5HMF-L* and *DielsAlder-L,* or, alternatively, to residual F-OH. More specifically, the peak at 885 cm^{-1} could be assigned to an asymmetric C-H stretching on the carbon forming the linkage with the polymeric structure (855.1 cm^{-1} in *Lin-L*), or to a combination between the asymmetric C-H stretching on the carbon forming the linkage and an asymmetric out-of-plane O-H bending inside the furan ring (852.8 cm^{-1} in *RingOp-L*). Instead, the peak at around 1149 cm^{-1} may corresponds to in plane C-H bending normal modes (namely 1149.0, 1159.4, 1172.6 cm^{-1} in *RingOp-C*, 1172.4 cm^{-1} *in StructFFL-C*), or, less probably, to a combination between C-H bending and C-O stretching in *Lin-L* (1160.4 cm^{-1}).

At last, the peak at 1505 cm^{-1} may corresponds also to the C = C symmetric stretching (1502.8 cm^{-1} and 1502.9 cm^{-1} in *Lin-L*, 1494.8 cm^{-1} and 1495.9 cm^{-1} in *RingOp-L*), see Table 1. Noteworthy, the negligible presence in the FTIR spectra of *ThS*-PFA of these three described normal modes, compared to *visc*-PFA, endorses the hypothesis that single-linked furans (e.g. *Lin-L* and *RingOp-L*) are missing or marginally present in *ThS*-PFA, in favour of more cross-linked furans (e.g. *Lin-C* and *RingOp-C*).

In the spectral range above 1500 cm^{-1}, i.e. the one where the FTIR curves are more similar, the presence of signals at ≈ 1710 cm^{-1} indicates the presence of ketones both in the *ThS*-PFA and *visc*-PFA chemical structures, as demonstrated in Ref. [29]. The presence of a bump at 1690–1670 cm^{-1} in *ThS*-PFA may indicate that the latter is affected by the presence of α,β unsatured ketones, which have the C = O stretching vibrational frequency shifted down to 40–60 cm^{-1} with respect to the saturated ones [52].

As expected, the DFT calculations confirm the presence of C = O stretching normal modes, although with slightly overestimated wavenumbers (1714.2 cm^{-1} and 1739.7 cm^{-1} for *RingOp-C*, 1737.6 cm^{-1} and 1751.9 cm^{-1} for *DielsAlder-C*, see Table 1). In fact it must be considered that hydrogen bonding, probably present in the polymeric structure, can reduce the frequency up to 40–60 cm^{-1} [52]. As described in Refs. [29–33] both *visc*-PFA and *ThS*-PFA contain a certain number of carbonyls deriving probably by opening-ring processes, which may also lead to keto-enol tautomerism and a consequent shift of the peaks of the functional groups involved towards lower wavenumbers, as it can be observed e.g. in acetylacetone [53], the enol and the keto form being more stable depending on the surrounding molecular environment [54]. This aspect will be subject of future research activities on PFA, in particular in connection with *RingOp-C*, *StructFFL-C* and *DielsAlder-C*.

When focusing the attention on the 650–850 cm^{-1} spectral range, we note that the experimental spectra of *ThS*-PFA and *visc*-PFA look like large doublets with maxima position at 728 cm^{-1} and 784 cm^{-1} for *ThS*-PFA, 736 cm^{-1} and 793 cm^{-1} for *visc*-PFA. The relative intensities between these two peaks change passing from *ThS*-PFA to *visc*-PFA.

If we observe the simulated FTIR spectrum *Lin*, we note that the lateral contribution (i.e. *Lin-L*) is characterized by an intense peak at 705.0 cm^{-1}, which is assigned to an out-of-plane symmetric C-H bending inside a single-linked furan ring, as shown above. Such a peak does not have a correspondent one relative to a double-linked furan ring, or rather, the correspondent ones are upshifted at 760.2 and 778.6 cm^{-1} (both in structure *Lin-C*). On the basis of these considerations, we can guess that the line-shape of this doublet can act as fingerprint for the relative presence of single-linked and double-linked furan rings inside the polymer network. In other words, the more intense is the peak at ≈ 730 cm^{-1} with respect to the one at ≈ 790 cm^{-1}, the more pronounced is the presence of single-linked furan rings. This is roughly

Table 1
Comparison between FTIR and Raman experimental peaks positions and simulated normal modes of *visc*-PFA and *ThS*-PFA, in the wavenumber range of 1450–1800 cm^{-1}. Legend: ν_S, symmetric stretching; ν_A, asymmetric stretching.

Visc-PFA exp. peak positions (cm^{-1})					ThS-PFA exp. peak positions (cm^{-1})						Simulated wavenumber (cm^{-1})	Normal mode description
FTIR	Raman exc. wavelength (nm)				FTIR	Raman exc. wavelength (nm)						
	1064	355	266	244		532	455	355	266	244		
1712					1711						1751.9	DielsAlder-C ν_S(C = O)
											1737.6	DielsAlder-C ν_A(C = O)
											1739.7	RingOp-C ν_S(C = O)
											1714.2	RingOp-C ν_A(C = O)
											1773.1	StructFFL-C ν (C = O) near O
											1776.2	StructFFL-C ν (C = O) near CH_3
	1650	1650	1652	1650	1680						1742.1	Struct5HMF-C ν (C = O)
											1648.6	Conj-C backbone-ν_A(C = C-C)
											1637.7	Conj-C backbone-ν_A(C = C-C)
1612					1611	1610	1610	1610	1610	1610	1612.1	RingOp-C ν(C = C)
											1610.8	Lin-C ring-ν_A(C = C)
1597	1597	1600	1600	1600							1595.1	Lin-L ring-ν_A(C = C)
											1594.5	Lin-L ring-ν_A(C = C)
											1588.9	RingOp-L ring-ν_A(C = C)
											1586.6	RingOp-L ring-ν_A(C = C)
											1602.1	StructFFL-L ring-ν_A(C = C)
											1601.4	S3HMF-L ring-ν_A(C = C)
											1592.9	DielsAlder-L ring-ν_A(C = C)
											1599.2	DielsAlder-L ring-ν_A(C = C)
											1600.2	DielsAlder-L ring-ν_A(C = C)
											1608.3	DielsAlder-L ring-ν_A(C = C)
											1602.9	Conj-L ring-ν_A(C = C)
		1577									1576.3	S5HM-C ring-ν_A(C = C)
1562	1563		1558	1562	1559	1570	1570		1550	1557	1555.0	Lin-C ring-ν_S(C = C)
											1547.8	Conj-C Coll. ring-ν_S(C = C-C)
											1541.3	Conj-C Coll. ring-ν_S(C = C-C)
	1528	1526									1517.6	S5HM-C ring-ν_S(C = C)
											1516.9	Conj-C Coll. ring-ν_S(C = C-C)
1505	1506	1491	1506	1506	1503	1483	1500	1500			1502.9	Lin-L ring-ν_S(C = C)
											1502.8	LinL ring-ν_S(C = C)
											1495.9	RingOp-L ring-ν_S(C = C)
											1494.8	RingOp-L ring-ν_S(C = C)
											1496.6	StructFFL-L ring-ν_S(C = C)
											1503.5	S3HMF-L ring-ν_S(C = C)
											1497.2	DielsAlder-L ring-ν_S(C = C)
											1498.3	DielsAlder-L ring-ν_S(C = C)
											1500.7	DielsAlder-L ring-ν_S(C = C)
											1502.9	DielsAlder-L ring-ν_S(C = C)

consistent with those FTIR peaks observed in the wavenumber range of 1050–1250 cm^{-1}, where the spectral difference between *ThS*-PFA and *visc*-PFA evidences the presence of a wide broad signal centred near 1150 cm^{-1}, this feature being consistent with the simulated one obtained from the structures *RingOp-C*, confirming that a greater cross linking occurs in the *ThS*-PFA with respect to the *visc*-PFA one. It is important to also note a coarse resemblance between the simulated *RingOp-C* and *DielsAlder-C* FTIR spectra. It may confirm that a large presence of *DielsAlder-C*, as reported by Tondi et al. [29] and by Falco et al. [31] in PFA prepared by a thermosetting procedure, could be present in *ThS*-PFA, although the FTIR is not able to discern the Diels-Alder structure from the others like *Lin-C* and *RingOp-C*. The presence of Diels Alder will be further discussed below, where Raman PFA spectra are compared with the simulated ones.

The FTIR spectra seem to exclude the possibility of a wide presence of *Conj-C*, both in *ThS*-PFA and in *visc*-PFA. The reasons for this assumption are two: firstly, the FTIR simulations of the *Conj-C* structure are characterized by two intense peaks at 1292.8 cm^{-1} and 1331.3 cm^{-1}, which are addressed to the C-H in-plane bending relative to the carbon atoms involved in the conjugation. Such simulated peaks are missing in the experimental FTIR spectra of both *ThS*-PFA and *visc*-PFA. Secondly, as shown in Fig. 6, the structure *Conj-C* is totally missing of vibrational peaks between 2800 and 3050 cm^{-1}. Since *ThS*-PFA and *visc*-PFA are characterized by an intense peak near 2900 cm^{-1}, we feel being able to exclude that *Conj-C* may constitute the principal component in both PFAs.

This is in agreement with the findings of our recent work for the *ThS*-PFA [29] and with the findings of Barsberg and co-authors [49], who predicted in PFA the presence of oligomers composed by non-conjugated aliphatic linked furan rings. More specifically, they declare that the spectral profile of PFA does not allow a unique assignment of the bands potentially ascribed to a conjugated structure. On the contrary, the works of Kim and co-authors [30,33], performed exploiting 325 nm RR, consider PFA mainly constituted of conjugated structures, where furan rings are linked each other in a way similar to our *Conj* structure. The fingerprint of this assignment, in their opinion, stands in the presence of an intense Raman band at 1650 cm^{-1}, which can be only addressed to the conjugated C = C stretching. In order to shed light about this discrepancy, we deepen in the following the peak assignment for the Raman spectra of *ThS*-PFA and *visc*-PFA, previously shown in Fig. 3.

4.3. Comparison between experimental and simulated Raman spectra

As seen in Fig. 3, the spectral changes occurring in the Raman spectra of both *visc*-PFA and *ThS*-PFA upon changes in the excitation wavelength suggest that, by changing excitation wavelength, different resonance conditions are encountered, in particular with excitation at 355 nm and 244 nm.

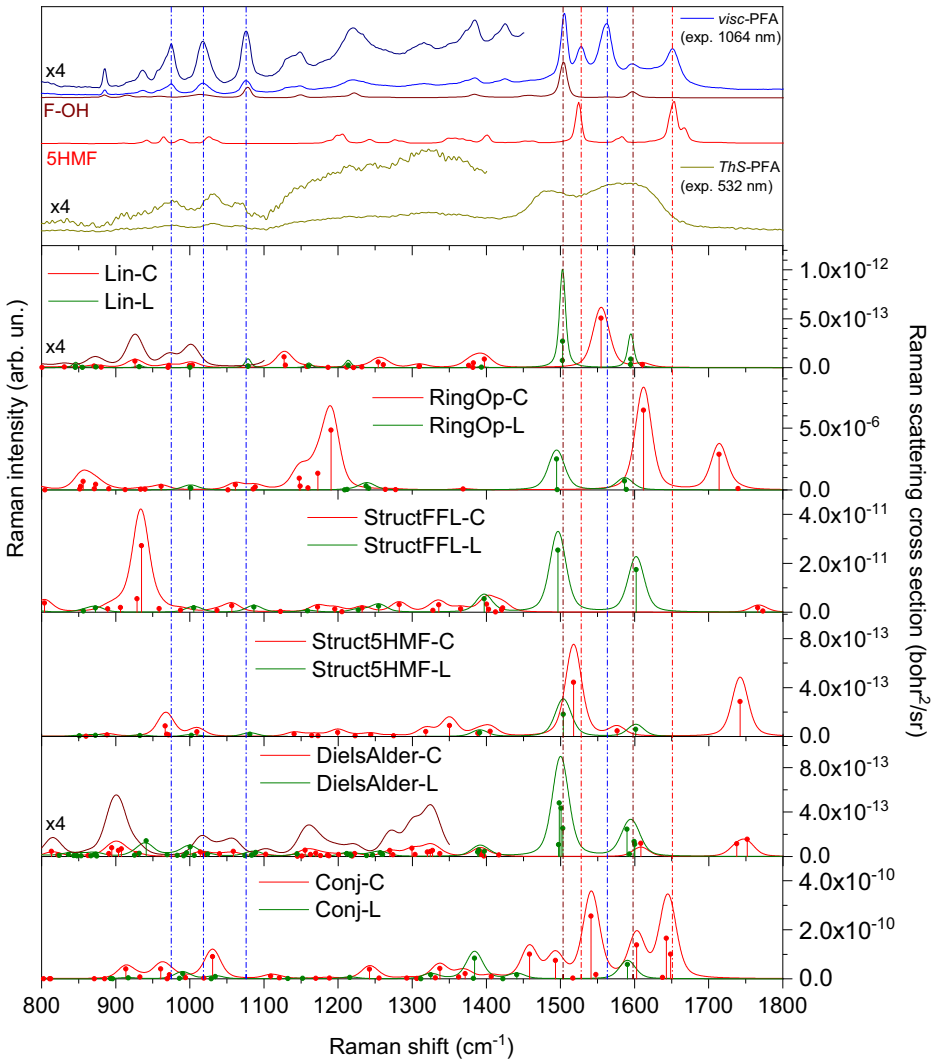

Fig. 7. Comparison of the experimental Raman spectra of *visc*-PFA and of *ThS*-PFA in the wavenumber ranges of 800–1800 cm^{-1}, recorded with excitation wavelengths of 1064 nm and 532 nm, and shown on the top, with the simulated Raman spectra obtained from the chemical structures *Lin*, *RingOp*, *StructFFL*, *Struct5HMF*, *DielsAlder* and *Conj* shown in Fig. 1, identifying in red the spectrum produced by the central (*-C*) portion of the chemical structures and in green the spectrum produced by the lateral (*-L*) one. In the top panel the F-OH (dark red) and 5HMF (red) experimental Raman spectra (1064 nm) are reported for comparison.

As done for the FTIR spectra, in Fig. 7 we compare the experimental Raman spectra of *visc*-PFA and *ThS*-PFA, recorded respectively at 1064 nm and at 532 nm, with the simulated Raman spectra obtained from the *Lin, RingOp, StructFFL, Struct5HMF, DielsAlder and Conj* chemical structures carried out with DFT(B-P86)/def2-SVP. Before starting the comparison between experimental and simulated Raman spectra, an important observation must be done. Differently to what occurs with FTIR, the Raman scattering cross section differs by orders of magnitude when passing through different simulated structures. For example, as seen in Fig. 7, the simulated Raman scattering cross section increases from 10^{-12} $bohr^2/sr$ for *Lin* to 10^{-6} $bohr^2/sr$ for *OpRing*. This is not a secondary aspect: it implies that some vibrational features from certain functional groups, which may be abundant in the PFA, may result to be hidden by the vibrational features coming from different functional groups that, taking advantage of their higher cross sections, are dominant in the final spectrum even if less abundant. This effect is exceedingly emphasized by resonance effects, making the spectral interpretation strongly conditioned by these aspects.

Differently to what occurs with FTIR, the Raman spectral profiles of *visc*-PFA and *ThS*-PFA in the wavenumber region between 1350 cm^{-1} and 1800 cm^{-1}, as seen on the top right of Fig. 7, are characterized by strong differences. With 1064 nm excitation the most intense Raman peak in *visc*-PFA is the one at 1506 cm^{-1}, which results to be also the sharpest one, with a FWHM bandwidth near 10 cm^{-1}. As already discussed for FTIR spectra, it is reasonable to exclude the presence of F-OH in the *ThS*-PFA sample. Therefore, in accordance with the FTIR results, we can deduce that the peaks are assigned to the symmetric C = C stretching of a furan ring like the ones of *Lin-L* and *RingOp-L* (simulated peaks at 1502.9 cm^{-1} and 1502.8 cm^{-1} for the *Lin-L*, 1495.9 cm^{-1} and 1494.8 cm^{-1} for *RingOp-L*, see Table 1). To better evidence the different sharpness of these peaks, we have simulated only the *Lin-L* employing a gaussian FWHM of 5 cm^{-1} instead of 10 cm^{-1}, as done throughout in this work (see Experimental paragraph). Furthermore, the *visc*-PFA contains a well-defined peak at around 1562 cm^{-1}, which can be easily addressed to the C = C symmetric stretching inside the furan ring double-linked to the polymer structure (simulated at 1555.0 cm^{-1} for the *Lin-C* structure, see Table 1). The predicted Raman cross section of these *Lin-C* normal modes, in particular $\approx 10^{-13}$ for 1555.0 cm^{-1} in *Lin-C*, is some order of magnitudes lower than the other simulated ones. Since the corresponding experimental peak at 1562 cm^{-1} is among the most intense in the *visc*-PFA spectra, we can confirm that, as seen with FTIR, *Lin-C* consti-

tute the main "building block" in the PFA structure. It is noteworthy that the analogue C = C symmetric stretching for the furanic ring single-linked to the polymer structure (i.e. *Lin-L*, *RingOp-L*, *StructFFL-L* and *DielsAlder-L*) is predicted to be between 1494 cm^{-1} and 1506 cm^{-1} (see Table 1 for more details).

Differently to what occurs in *ThS*-PFA, the *visc*-PFA 1064 nm Raman spectrum evidences the presence of an intense isolated peak at around 1650 cm^{-1}. Such a peak is accompanied by an analogue well defined peak at around 1528 cm^{-1}, missing in *ThS*-PFA. As reported further, Kim and co-workers [30,32,33,55] assigned this peak to the asymmetric C = C-C stretching between two furanic rings. Our simulations report for the *Conj-C* structure a peak position for the normal modes centred at 1648.6 and 1637.7 cm^{-1} (addressed to the backbone C = C-C stretching, see Table 1), as well as the peak at 1541.3 cm^{-1}, which is a normal mode that includes collective C-C stretching inside and outside the furanic ring. Although the first is well close to 1650 cm^{-1}, the latter is approximately 15 cm^{-1} above the experimental one at 1528 cm^{-1}. In addition to the previous consideration carried out during the interpretation of the FTIR spectra, which aims to exclude the presence of *Conj-C* structures, it is noteworthy that the peaks at 1650 cm^{-1} and 1528 cm^{-1} strongly resemble the ones of 5HMF at 1655 cm^{-1} and 1524 cm^{-1}. It is reasonable to suppose that these peaks can be addressed to the *Struct5HMF-C* structure shown in Fig. 1. Considering the simulation, the symmetric C = O stretching of *Struct5HMF-C* is calculated to be at 1742.2 cm^{-1}, while the furan ring symmetric C = C stretching is at 1517.4 cm^{-1}. The calculated C = O stretching peak is actually far from the experimental one. However, such a discrepancy occurs also for the predicted 5HMF C = O, while the other peaks are well reproduced in wavenumbers, as evidenced by observing the comparison between simulated and experimental FTIR and Raman spectra of 5HMF shown in the Supplementary Materials. Nevertheless, it is the agreement with the *experimental* 5HMF spectrum which reinforces the attribution of the peaks at 1650 cm^{-1} and 1526 cm^{-1} to the *Struct5HMF-C* structure. According to all these considerations, we can exclude the presence of conjugated structures for the *visc*-PFA and for the *ThS*-PFA.

To further confirm this interpretation of the spectra, in Fig. 8 we compare the Raman spectra of *visc*-PFA and *ThS*-PFA, collected employing 355 nm incident laser radiation, with the spectral simulations carried out at the same wavelength for *Lin*, *RingOp*, *StructFFL*, *Struct5HMF*, *DielsAlder* and *Conj*. At this excitation wavelength the two experimental peaks at 1650 cm^{-1} and 1526 cm^{-1} in *visc*-PFA result to be strongly enhanced with respect to all the other ones. Noteworthy, such peaks are completely missed in the *ThS*-PFA spectrum, which instead has two broadened peaks at ≈ 1610 cm^{-1} and ≈1500 cm^{-1}. It confirms the absence of *Struct5HMF-C* in the *ThS*-PFA, in addition to the absence of conjugation type *Conj,* as recently demonstrated [29].

In Fig. 8 it is also reported the experimental spectrum of 5HMF collected at 355 nm. At this excitation wavelength the agreement between the 5HMF and *visc*-PFA spectral lineshapes is more precise with respect to the one evidenced in Fig. 7 at 1064 nm. Apart from the already mentioned matches of the peaks at 1650 cm^{-1} and 1528 cm^{-1}, we also have a correspondence between the broad signal of the *visc*-PFA at ≈ 1575 cm^{-1} with the signal of 5HMF at 1580 cm^{-1}, as well as the correspondence between the *visc*-PFA peak at ≈ 1020 cm^{-1} and the one of 5HMF at ≈ 1023 cm^{-1}. By comparison with the calculated spectra we assign the peak at 1575 cm^{-1} to asymmetric C = C stretching inside the *Struct5HMF-C* furan ring, with the calculated one at 1576.3 cm^{-1} (note that *Lin-L* ones were at 1594.5 cm^{-1} and 1595.1 cm^{-1} while *Lin-C* ones at 1610.8 cm^{-1}, see Table 1), while the experimental peak at 1020 cm^{-1} can be probably assigned to the simulated normal mode at 1009.5 cm^{-1}, assigned to *Struct5HMF-C* C-H bending, as further discussed below in the text. In is important to note how, although *Struct5HMF* is not the most relevant component of *visc*-PFA, the Resonance Raman effect at 355 nm enhances the *Struct5HMF* vibrational peaks of the whole *visc*-PFA spectrum with respect to the others component. On the contrary, the lack of Raman peaks at 1650 cm^{-1} and 1528 cm^{-1} in the *ThS*-PFA spectrum is indicative of the *Struct5HMF* absence.

In contrast to what occurs for *visc*-PFA, the interpretation of the spectrum of *ThS*-PFA is less straight forward, because of the intrinsic broadening of the Raman peaks. While the spectral interpretation results to be not unique in the visible range, because of the overlapping on many normal modes, moving to 355 nm the Raman resonance effect favours the enhancing of few vibrational features, allowing a more accurate peak assignation when also employing the complementary information contained in the FTIR spectra. More specifically, the broad peak at ≈1610 cm^{-1} can be reasonably assigned to the *RingOp-C* normal mode at 1612.1 cm^{-1}, while the left peak tail includes the *Lin-C* one at 1555.0 cm^{-1} (see Table 1). The peak at around 1500 cm^{-1} can be instead assigned to *Lin-L* and *RingOp-L*, as done for *visc*-PFA, and to *DielsAlder-L*. Particularly interesting is the fact that at an excitation wavelength of 532 nm, differently to what occurs in *visc*-PFA, the peak is down shifted by 20 cm^{-1} and results to be more broadened with respect to the analogue one in *visc*-PFA (see Fig. 7). The signal broadening can be considered as a sign of the increased complexity of the polymeric structure, caused by a more pronounced cross-linking. A similar increase of cross linking was observed by Falco et al. [31] in thermosetted PFA, which supposed also the formations of several functional groups during the polymerization process besides the one modelled in the present work, such as isopropyl and furfuryl levulinate, as well as methylene linkages, easy to be detect with NMR, but not so easy to be discerned from other structures by means of vibrational spectroscopies.

It is also noteworthy to observe how the *DielsAlder-L* normal modes relative to the furan rings symmetric C = C stretching are distributed from 1497 to 1503 cm^{-1} (see details in Table 1). This indicates that, as already guessed analysing the FTIR spectra, from viscous to thermosetted PFA, the polymer passes from a structure formed by short polymer chains composed by *Lin*, *RingOp*, *Struct5HMF* and *DielsAlder* units, to a polymeric cross-linked structure mainly formed by *Lin-C*, *DielsAlder-C* and *RingOp-C* units, where few lateral structures (namely *Lin-L*, *RingOp-L* and *DielsAlder-L*) are present and *Struct5HMF* completely disappears.

The Resonance Raman spectra with 266 nm laser excitation (Fig. 9) further confirm the peaks attributions performed so far, although the increased presence of electronic transitions close to this excitation wavelength (see Fig. 4) probably leads to a lower accuracy of the RR effect and consequently to a poorer estimation of the peak's intensities. The novelty in term of spectral information at 266 nm is the possibility to get a good spectral interpretation of the region below 1300 cm^{-1} because, differently to what occurs in the visible range and at 355 nm, the relative spectral intensity of the lower part of the spectrum is almost comparable with the higher one. It is interesting to observe how in the wavenumber range of 900–1100 cm^{-1} the Raman spectral profile in both *visc*-PFA and *ThS*-PFA strongly resembles the simulated *Lin-C* spectral profile, with two peaks centred at around 970 cm^{-1} and 1018 cm^{-1}, slightly underestimated in wavenumber, as already found in the analogue simulations carried out for F-OH to test the simulation's reliability. It is also interesting to note how the experimental peak at 1018 cm^{-1} found in the Raman spectra of *visc*-PFA and *Ths*-PFA is slightly upshifted with respect to the analogue one found in F-OH (1015 cm^{-1}). Moreover, the F-OH Raman peaks at ≈ 930 cm^{-1}, ≈ 1080 cm^{-1} and 1155 cm^{-1} disappear in the PFA Raman spectra at 266 nm, confirming that the experimental PFA Resonant

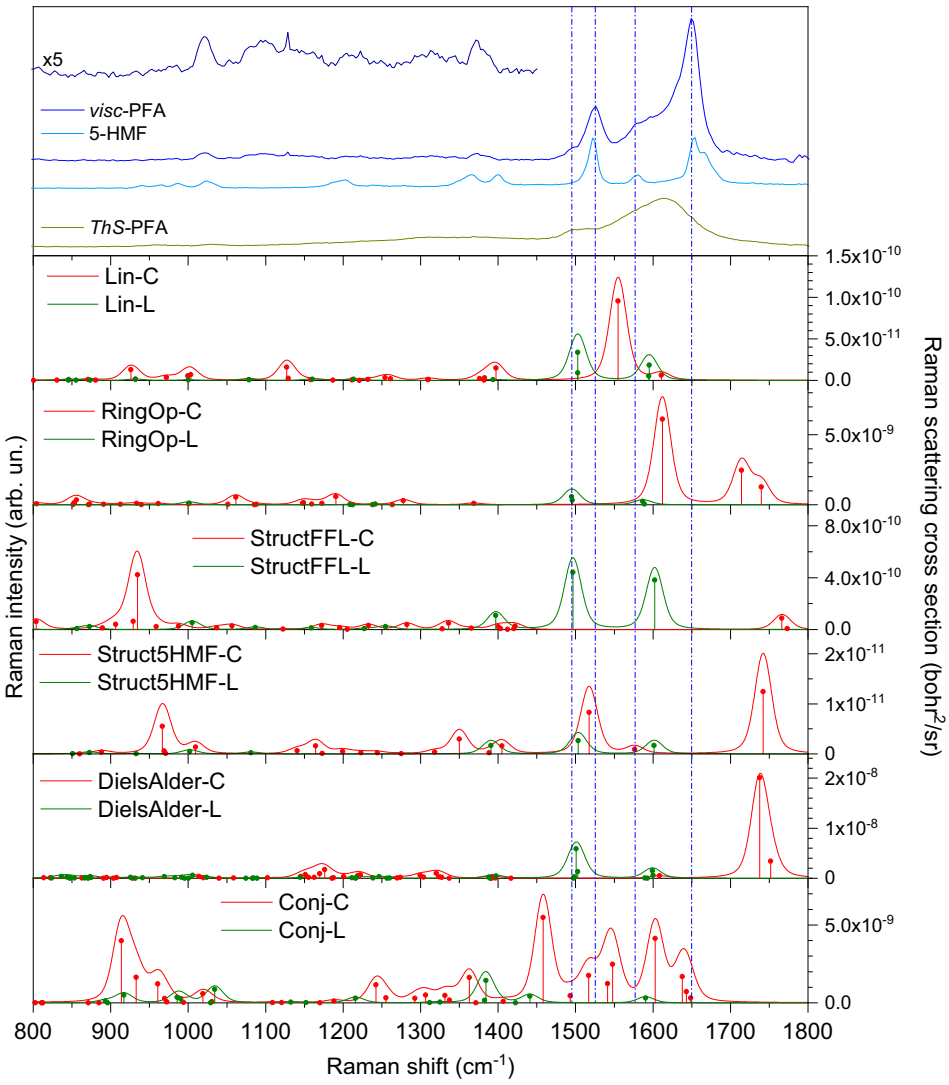

Fig. 8. Comparison of the experimental Raman spectra of *visc*-PFA and of *ThS*-PFA in the wavenumber range of 800–1800 cm^{-1}, recorded with the excitation wavelength of 355 nm, and shown on the top, with the simulated Raman spectra obtained from the chemical structures *Lin*, *RingOp*, *StructFFL*, *Struct5HMF*, *DielsAlder* and *Conj* shown in Fig. 1, identifying in red the spectrum produced by the central (*-C*) portion of the chemical structures and in green the spectrum produced by the lateral (*-L*) one.

Raman peaks at 970 cm^{-1} and 1018 cm^{-1} cannot be attributed to residual F-OH.

At the laser excitation wavelength of 244 nm (Fig. 10), we observe the disappearance of the peaks at around 1650 cm^{-1}, 1610 cm^{-1} and 1526 cm^{-1}, characterized by the Resonance Raman enhancement at 355 nm. The two peaks at 970 cm^{-1} and 1018 cm^{-1} result to be still present in both PFAs, while the upper part of the spectrum includes, as principal spectral features, a peak at 1562 cm^{-1} for *visc*-PFA and at 1557 cm^{-1} for *ThS*-PFA. The simulation results show how the Raman spectral profiles in both PFAs resemble the one of *Lin-C*, in perfect agreement with the findings from the previous analysis done for the other wavelengths and from FTIR. Small differences in the experimental Raman spectral profiles can be found within *visc*-PFA and *ThS*-PFA, mainly differing by the size of the structure centred at around 1610 cm^{-1}. It is reasonable to suppose that such feature comes from the aforementioned *RingOp-C* normal mode simulated at 1612.1 cm^{-1} or, alternatively, to the analogue C = C stretching vibration occurring in the Diels-Alder structure of *DielsAlder-C* (1608.3 cm^{-1}), see Table 1. In this case the higher calculated Raman cross section of the *DielsAlder-C* normal mode with respect to the *RingOp-C* one can justify why the analogue peak in the *visc*-PFA is strongly reduced in intensity with respect to the one in *ThS*-PFA. This is someway in agreement to what was found in Ref. [29] about the relevant presence of *DielsAlder-C* in *ThS*-PFA.

4.4. Reliability of simulated Raman spectra

The spectral analysis process has evidenced how the nature of π bonds outside the furan ring (in particular those of the C = C or conjugation in the cross-linked structure) is successfully investigated by Resonant Raman spectroscopy. In particular, RR performed at 355 nm was able to detect the presence of C = C in the cross-linked structures and, more important, to distinguish their chemical conformation. On the other side, FTIR has resulted to be fundamental to investigate the oxidation level of PFA samples as well as to infer about residual F-OH present in PFA.

However, the comparison between the experimental and theoretical FTIR and Raman spectra evidences a moderate disagreement for the signals arising from the C = C and C = O normal modes, especially in RR. We speculate that this disagreement might be assigned, in decreasing order of importance, to

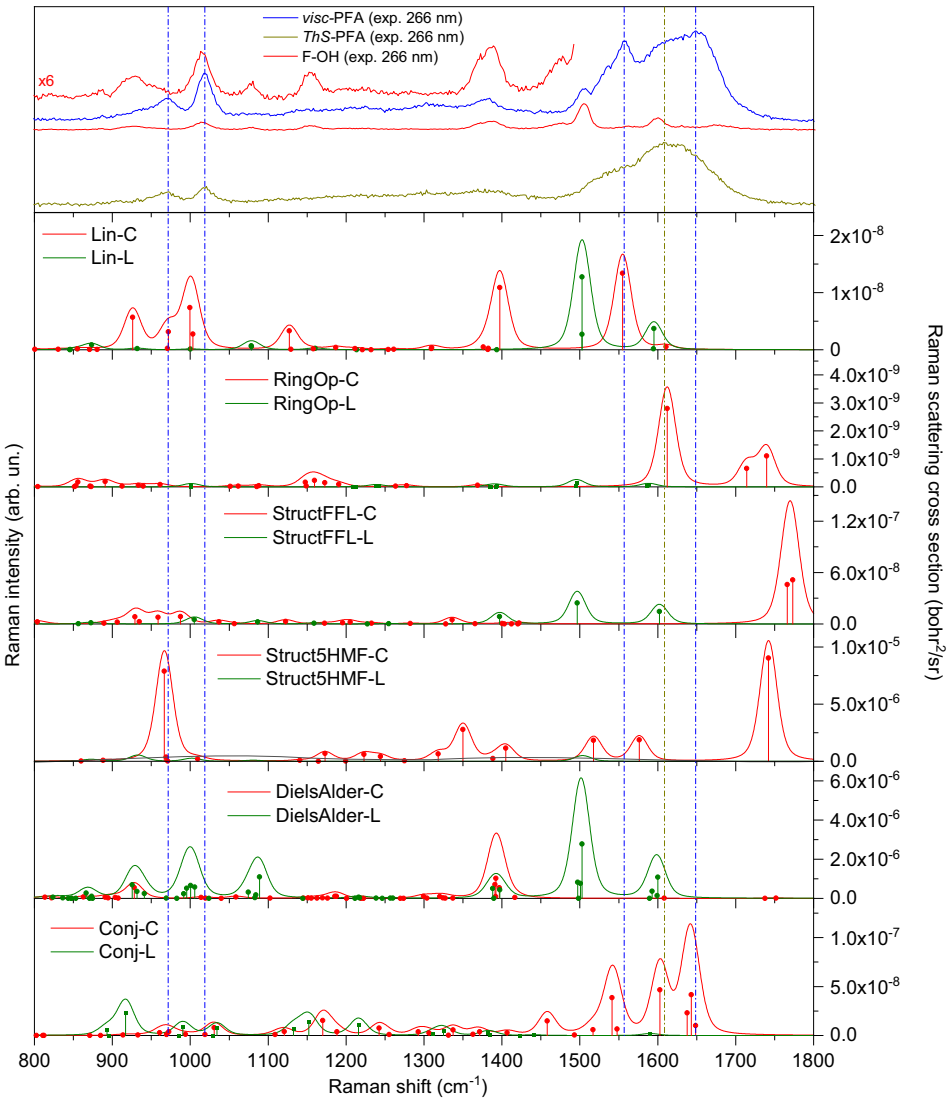

Fig. 9. Comparison of the experimental Raman spectra of *visc*-PFA and of *ThS*-PFA in the wavenumber range of 800–1800 cm^{-1}, recorded with the excitation wavelength of 266 nm, and shown on the top, with the calculated Raman spectra obtained from the chemical structures *Lin*, *RingOp*, *StructFFL*, *Struct5HMF*, *DielsAlder* and *Conj* shown in Fig. 1, identifying in red the spectrum produced by the central (*-C*) portion of the chemical structures and in green the spectrum produced by the lateral (*-L*) one .

1. The coarse chemical mode, that does not take into account the possible presence of other components
2. Conformational effects, solid state (periodic boundary) and packing effects, which have not been considered in the study
3. The theoretical spectral intensity model that does not cover electronic Raman *resonance* effects and consequently the theoretical predictions of RR cross sections are expected to deviate
4. The occurrence of multiple sites of hydrogen bonds could also be a secondary source for quantitative disagreements between experiment and theory.

However, a substantial improvement of the electronic structure model (the local density functional BP-86) in order to provide a more accurate description of the hydrogen bonds seems to be contraindicated, given the complexity of the polymer and the marginal effect expected from this factor 4. with respect to factors 1., 2. and 3.

In summary, simulations are able to provide significative, but only qualitative information about the origins of the electronic transitions occurring between 300 and 350 nm, addressed to presence of C = C polymer moieties. It is fundamental to further highlight the extreme sensitivity of C = C normal modes to RR excited at around 350 nm, also confirmed by the theoretical results, providing cross sections one order of magnitude larger with respect to the ones calculated for structure *Lin*, for example, which is probably the predominant one in both the PFA types. This aspect has to be taken in serious consideration when performing spectral interpretation. More specifically, if complementary measurements of vibrational spectra (i.e. considering both FTIR and Raman) are not performed, an overestimation of the presence of the resonant structures could be wrongly deduced.

5. Conclusions

The comparison between simulated and experimental FTIR, Raman and Resonance Raman spectra evidences how the linear *Lin-C* structure is the dominant in PFA, in agreement with [29]. However, while *visc*-PFA is formed by small furan oligomers, with a low degree of polymerization, *ThS*-PFA is characterized by a more pronounced cross-linking. In addition, a certain amount of 5-methylfurfural derived structures as well as unreacted F-OH is present in *visc*-PFA, both disappearing in *ThS*-PFA.

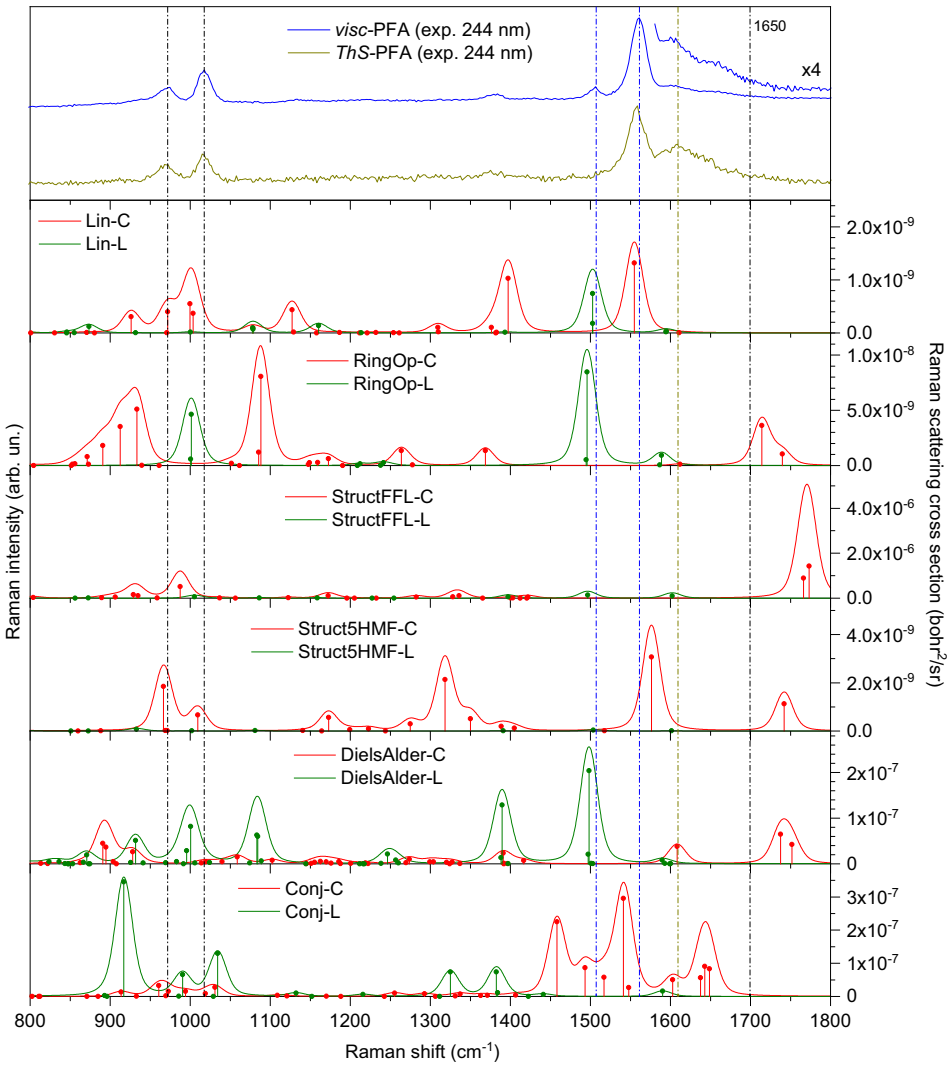

Fig. 10. Comparison of the experimental Raman spectra of *visc*-PFA and of *ThS*-PFA in the wavenumber range of 800–1800 cm^{-1}, recorded with the excitation wavelength of 244 nm, and shown on the top, with the simulated Raman spectra obtained from the chemical structures *Lin*, *RingOp*, *StructFFL*, *Struct5HMF*, *DielsAlder* and *Conj* shown in Fig. 1, identifying in red the spectrum produced by the central (*-C*) portion of the chemical structures and in green the spectrum produced by the lateral (*-L*) one.

Furthermore, both *visc*-PFA and *ThS*-PFA contain an unspecified number of carbonyls and C = C bonds (similar to that of *RingOp-C*), deriving probably by opening-ring processes, as observed in Ref. [29–33]. Most important, the presence of conjugated structures can be excluded, both in *visc*-PFA and in *ThS*-PFA.

It is also reasonable to suppose that a certain amount of *DielsAlder-C* structure is included in the cross-linked structure of *ThS*-PFA. However, the information coming from FTIR and Raman are not sufficient to disentangle the *DielsAlder-C* contribution from the *Lin-C* and *RingOp-C* ones, since their simulations provide similar results in terms of normal mode frequency and intensity.

The spectral interpretation process, carried out comparing the experimental spectra with the simulated ones, evidences how a broad, complete and reliable characterization of such a complex polymer structure, free from spectral misinterpretations, can be only obtained by the complementary use of both FTIR, Raman and Resonance Raman spectroscopy.

CRediT authorship contribution statement

Francesco D'Amico: Methodology, Investigation, Resources, Writing - review & editing, Supervision. **Maurizio E. Musso:** Methodology, Investigation, Resources, Writing - review & editing. **Raphael J.F. Berger:** Quantum Mechanical Simulations. **Nicola Cefarin:** Investigation. **Giovanni Birarda:** Investigation. **Gianluca Tondi:** Methodology, Investigation, Resources, Writing - review & editing, Supervision. **Durval Bertoldo Menezes:** Investigation. **Andreas Reyer:** Investigation. **Letizia Scarabattoli:** Investigation. **Thomas Sepperer:** Methodology. **Thomas Schnabel:** Supervision. **Lisa Vaccari:** Supervision, Writing - review & editing, Project administration.

Declaration of Competing Interest

The authors declare that they have no known competing financial interests or personal relationships that could have appeared to influence the work reported in this paper.

Acknowledgments

The authors would like to acknowledge the financial support provided by the European Regional Development Fund and Interreg V-A Italy Austria 2014–2020 through the Interreg Italy Austria

project ITAT 1023 InCIMa "Smart Characterization of Intelligent Materials".

Appendix A. Supplementary material

Supplementary data to this article can be found online at https://doi.org/10.1016/j.saa.2021.120090.

References

[1] A. Gandini, Polymers from Renewable Resources: A Challenge for the Future of Macromolecular Materials, Macromolecules. 41 (2008) 9491–9504, https://doi.org/10.1021/ma801735u.

[2] M.G. Alimukhamedov, F.A. Magrupov, Kinetics of homopolycondensation of furfuryl alcohol, Polym. Sci. Ser. B. 49 (2007) 167–171, https://doi.org/10.1134/S1560090407070019.

[3] C.R. Schmitt, Polyfurfuryl Alcohol Resins, Polym.-Plast. Technol. Eng. 3 (1974) 121–158, https://doi.org/10.1080/03602557408545025.

[4] A.P. Dunlop, F.N. Peters, The furans, Reinhold Publishing Corporation, New York, 1953.

[5] G. Machado, S. Leon, F. Santos, R. Lourega, J. Dullius, M.E. Mollmann, P. Eichler, Literature Review on Furfural Production from Lignocellulosic Biomass, Nat. Resour. 7 (2016) 115–129, https://doi.org/10.4236/nr.2016.73012.

[6] A.O. Iroegbu, S.P. Hlangothi, Furfuryl Alcohol a Versatile, Eco-Sustainable Compound in Perspective, Chem. Afr. 2 (2019) 223–239, https://doi.org/10.1007/s42250-018-00036-9.

[7] R.F. Perez, M.A. Fraga, Hemicellulose-derived chemicals: one-step production of furfuryl alcohol from xylose, Green Chem. 16 (2014) 3942–3950, https://doi.org/10.1039/C4GC00398E.

[8] A. Gardziella, A. Kwasniok, H. Heerdegen, G. Janocha, Furfuryl alcohol binders, methods for their production and use, US4634723A, 1987. https://patents.google.com/patent/US4634723A/en?oq=4634723 (accessed February 11, 2021).

[9] M. Holtzer, S. Żymankowska-Kumon, A. Bobrowski, R. Dańko, A. Kmita, The influence of reclaim addition on the emission of PAHs and BTEX from moulding sands with furfuryl resin with the average amount of furfuryl alcohol, Arch. Foundry Eng. 14 (2014) 37–42.

[10] P. Luckeneder, J. Gavino, R. Kuchernig, A. Petutschnigg, G. Tondi, Sustainable Phenolic Fractions as Basis for Furfuryl Alcohol-Based Co-Polymers and Their Use as Wood Adhesives, Polymers. 8 (2016) 396, https://doi.org/10.3390/polym8110396.

[11] H. Deka, M. Misra, A. Mohanty, Renewable resource based "all green composites" from kenaf biofiber and poly(furfuryl alcohol) bioresin, Ind. Crops Prod. 41 (2013) 94–101, https://doi.org/10.1016/j.indcrop.2012.03.037.

[12] G. Nanni, J.A. Heredia-Guerrero, U.C. Paul, S. Dante, G. Caputo, C. Canale, A. Athanassiou, D. Fragouli, I.S. Bayer, Poly(furfuryl alcohol)-Polycaprolactone Blends, Polymers. 11 (2019) 1069, https://doi.org/10.3390/polym11061069.

[13] B.O. Ribeiro, V.S. Valério, A. Gandini, T.M. Lacerda, Copolymers of xylan-derived furfuryl alcohol and natural oligomeric tung oil derivatives, Int. J. Biol. Macromol. 164 (2020) 2497–2511, https://doi.org/10.1016/j.ijbiomac.2020.08.095.

[14] L. Sommerauer, J. Grzybek, M.S. Elsaesser, A. Benisek, T. Sepperer, E. Dachs, N. Hüsing, A. Petutschnigg, G. Tondi, Furfuryl Alcohol and Lactic Acid Blends: Homo- or Co-Polymerization?, Polymers 11 (2019) 1533, https://doi.org/10.3390/polym11101533.

[15] J.-M. Pin, N. Guigo, L. Vincent, N. Sbirrazzuoli, A. Mija, Copolymerization as a Strategy to Combine Epoxidized Linseed Oil and Furfuryl Alcohol: The Design of a Fully Bio-Based Thermoset, ChemSusChem. 8 (2015) 4149–4161, https://doi.org/10.1002/cssc.201501259.

[16] J. Eckardt, J. Neubauer, T. Sepperer, S. Donato, M. Zanetti, N. Cefarin, L. Vaccari, M. Lippert, M. Wind, T. Schnabel, A. Petutschnigg, G. Tondi, Synthesis and Characterization of High-Performing Sulfur-Free Tannin Foams, Polymers. 12 (2020) 564, https://doi.org/10.3390/polym12030564.

[17] G. Tondi, M. Link, C. Kolbitsch, R. Lesacher, A. Petutschnigg, Pilot plant up-scaling of tannin foams, Ind. Crops Prod. 79 (2016) 211–218, https://doi.org/10.1016/j.indcrop.2015.11.013.

[18] A. Reyer, G. Tondi, R.J.F. Berger, A. Petutschnigg, M. Musso, Raman spectroscopic investigation of tannin-furanic rigid foams, Vib. Spectrosc. 84 (2016) 58–66, https://doi.org/10.1016/j.vibspec.2016.03.005.

[19] G. Tondi, M. Link, C. Kolbitsch, J. Gavino, P. Luckeneder, A. Petutschnigg, R. Herchl, C. van Doorslaer, Lignin-based foams: production process and characterization, BioResources. 11 (2016) 2972–2986.

[20] N. Guigo, A. Mija, L. Vincent, N. Sbirrazzuoli, Eco-friendly composite resins based on renewable biomass resources: Polyfurfuryl alcohol/lignin thermosets, Eur. Polym. J. 46 (2010) 1016–1023, https://doi.org/10.1016/j.eurpolymj.2010.02.010.

[21] M. Choura, N.M. Belgacem, A. Gandini, Acid-Catalyzed Polycondensation of Furfuryl Alcohol: Mechanisms of Chromophore Formation and Cross-Linking, Macromolecules. 29 (1996) 3839–3850, https://doi.org/10.1021/ma951522f.

[22] X. Zhang, D.H. Solomon, The reaction of furfuryl alcohol resins with hexamethylenetetramine: A 13C and 15N high-resolution solid-state NMR study, J. Polym. Sci. Part B Polym. Phys. 35 (1997) 2233–2243, https://doi.org/10.1002/(SICI)1099-0488(199710)35:14<2233::AID-POLB4>3.0.CO;2-X.

[23] R. González, J.M. Figueroa, H. González, Furfuryl alcohol polymerisation by iodine in methylene chloride, Eur. Polym. J. 38 (2002) 287–297, https://doi.org/10.1016/S0014-3057(01)00090-8.

[24] H. Wang, J. Yao, Use of Poly(furfuryl alcohol) in the Fabrication of Nanostructured Carbons and Nanocomposites, Ind. Eng. Chem. Res. 45 (2006) 6393–6404, https://doi.org/10.1021/ie0602660.

[25] S. Lande, M. Westin, M. Schneider, Properties of furfurylated wood, Scand. J. For. Res. 19 (2004) 22–30, https://doi.org/10.1080/0282758041001915.

[26] R.T. Conley, I. Metil, An investigation of the structure of furfuryl alcohol polycondensates with infrared spectroscopy, J. Appl. Polym. Sci. 7 (1963) 37–52, https://doi.org/10.1002/app.1963.070070104.

[27] E.M. Wewerka, Study of the γ-alumina polymerization of furfuryl alcohol, J. Polym. Sci. [A1]. 9 (1971) 2703–2715. https://doi.org/10.1002/pol.1971.150090923 .

[28] I.S. Chuang, G.E. Maciel, G.E. Myers, Carbon-13 NMR study of curing in furfuryl alcohol resins, Macromolecules. 17 (1984) 1087–1090, https://doi.org/10.1021/ma00135a019.

[29] G. Tondi, N. Cefarin, T. Sepperer, F. D'Amico, R.J.F. Berger, M. Musso, G. Birarda, A. Reyer, T. Schnabel, L. Vaccari, Understanding the Polymerization of Polyfurfuryl Alcohol: Ring Opening and Diels-Alder Reactions, Polymers. 11 (2019) 2126, https://doi.org/10.3390/polym11122126.

[30] T. Kim, R.S. Assary, H. Kim, C.L. Marshall, D.J. Gosztola, L.A. Curtiss, P.C. Stair, Effects of solvent on the furfuryl alcohol polymerization reaction: UV Raman spectroscopy study, Catal. Today. 205 (2013) 60–66, https://doi.org/10.1016/j.cattod.2012.09.033.

[31] G. Falco, N. Guigo, L. Vincent, N. Sbirrazzuoli, Opening Furan for Tailoring Properties of Bio-based Poly(Furfuryl Alcohol) Thermoset, ChemSusChem. 11 (2018) 1805–1812, https://doi.org/10.1002/cssc.201800620.

[32] T. Kim, J. Jeong, M. Rahman, E. Zhu, D. Mahajan, Characterizations of furfuryl alcohol oligomer/polymerization catalyzed by homogeneous and heterogeneous acid catalysts, Korean J. Chem. Eng. 31 (2014) 2124–2129, https://doi.org/10.1007/s11814-014-0322-x.

[33] T. Kim, R.S. Assary, C.L. Marshall, D.J. Gosztola, L.A. Curtiss, P.C. Stair, Acid-Catalyzed Furfuryl Alcohol Polymerization: Characterizations of Molecular Structure and Thermodynamic Properties, ChemCatChem. 3 (2011) 1451–1458, https://doi.org/10.1002/cctc.201100098.

[34] https://www.polysciences.com/default/polyfurfuryl-alcohol (accessed March 29, 2021)..

[35] F. D'Amico, M. Saito, F. Bencivenga, M. Marsi, A. Gessini, G. Camisasca, E. Principi, R. Cucini, S. Di Fonzo, A. Battistoni, E. Giangrisostomi, C. Masciovecchio, UV resonant Raman scattering facility at Elettra, Nucl. Instrum. Methods Phys. Res. Sect. Accel. Spectrometers Detect. Assoc. Equip. 703 (2013) 33–37, https://doi.org/10.1016/j.nima.2012.11.037.

[36] F. Neese, Prediction of molecular properties and molecular spectroscopy with density functional theory: From fundamental theory to exchange-coupling, Coord. Chem. Rev. 253 (2009) 526–563, https://doi.org/10.1016/j.ccr.2008.05.014.

[37] F. Neese, A critical evaluation of DFT, including time-dependent DFT, applied to bioinorganic chemistry, JBIC J. Biol. Inorg. Chem. 11 (2006) 702–711, https://doi.org/10.1007/s00775-006-0138-1.

[38] F. Neese, Software update: the ORCA program system, version 4.0, WIREs Comput, Mol. Sci. 8 (2018), https://doi.org/10.1002/wcms.1327 e1327.

[39] F. Neese, The ORCA program system, WIREs Comput. Mol. Sci. 2 (2012) 73–78, https://doi.org/10.1002/wcms.81.

[40] A.D. Becke, Density-functional thermochemistry. IV. A new dynamical correlation functional and implications for exact-exchange mixing, J. Chem. Phys. 104 (1996) 1040–1046, https://doi.org/10.1063/1.470829.

[41] A.D. Becke, Density-functional thermochemistry. III. The role of exact exchange, J. Chem. Phys. 98 (1993) 5648–5652, https://doi.org/10.1063/1.464913.

[42] C. Lee, W. Yang, R.G. Parr, Development of the Colle-Salvetti correlation-energy formula into a functional of the electron density, Phys. Rev. B. 37 (1988) 785–789, https://doi.org/10.1103/PhysRevB.37.785.

[43] R. Krishnan, J.S. Binkley, R. Seeger, J.A. Pople, Self-consistent molecular orbital methods. XX. A basis set for correlated wave functions, J. Chem. Phys. 72 (1980) 650–654, https://doi.org/10.1063/1.438955.

[44] M.J. Frisch, J.A. Pople, J.S. Binkley, Self-consistent molecular orbital methods 25. Supplementary functions for Gaussian basis sets, J. Chem. Phys. 80 (1984) 3265–3269, https://doi.org/10.1063/1.447079.

[45] P.J. Stephens, N. Harada, ECD cotton effect approximated by the Gaussian curve and other methods, Chirality. 22 (2010) 229–233, https://doi.org/10.1002/chir.20733.

[46] R. Ahlrichs, M. Bär, M. Häser, H. Horn, C. Kölmel, Electronic structure calculations on workstation computers: The program system turbomole, Chem. Phys. Lett. 162 (1989) 165–169, https://doi.org/10.1016/0009-2614(89)85118-8.

[47] D.A. Long, Raman spectroscopy, McGraw-Hill, New York; London, 1977.

[48] A. Weber, Raman spectroscopy of gases and liquids, Springer, 1979.

[49] S. Barsberg, L.G. Thygesen, Poly(furfuryl alcohol) formation in neat furfuryl alcohol and in cymene studied by ATR-IR spectroscopy and density functional theory (B3LYP) prediction of vibrational bands, Vib. Spectrosc. 49 (2009) 52–63, https://doi.org/10.1016/j.vibspec.2008.04.013.

[50] 2-Hydroxymethylfuran - FTIR - Spectrum - SpectraBase, (n.d.). https://spectrabase.com/spectrum/6y6PEQFf35D (accessed March 19, 2021).

[51] H. Ipakchi, A. Shegeft, A.M. Rezadoust, M.J. Zohuriaan-Mehr, K. Kabiri, S. Sajjadi, Bio-resourced furan resin as a sustainable alternative to petroleum-based phenolic resin for making GFR polymer composites, Iran. Polym. J. 29 (2020) 287–299, https://doi.org/10.1007/s13726-020-00793-w.
[52] G. Socrates, Infrared and Raman Characteristic Group Frequencies: Tables and Charts, 3rd Edition., Wiley, 2004.
[53] H. Wang, H. Xu, Q. Liu, X. Zheng, The noncoincidence phenomenon of acetonylacetone CO stretching in a binary mixture and the aggregation-induced split theory, RSC Adv. 10 (2020) 30982–30989, https://doi.org/10.1039/D0RA02932G.
[54] V. Feyer, K.C. Prince, M. Coreno, S. Melandri, A. Maris, L. Evangelisti, W. Caminati, B.M. Giuliano, H.G. Kjaergaard, V. Carravetta, Quantum Effects for a Proton in a Low-Barrier, Double-Well Potential: Core Level Photoemission Spectroscopy of Acetylacetone, J. Phys. Chem. Lett. 9 (2018) 521–526, https://doi.org/10.1021/acs.jpclett.7b03175.
[55] T. Kim, R.S. Assary, L.A. Curtiss, C.L. Marshall, P.C. Stair, Vibrational properties of levulinic acid and furan derivatives: Raman spectroscopy and theoretical calculations, J. Raman Spectrosc. 42 (2011) 2069–2076, https://doi.org/10.1002/jrs.2951.